Inhibition of Haspin Kinase Promotes Cell-Intrinsic and Extrinsic Antitumor Activity

Johannes C. Melms[1,2,3,4], Sreeram Vallabhaneni[1,2], Caitlin E. Mills[5], Clarence Yapp[5], Jia-Yun Chen[5], Eugenio Morelli[1], Patricia Waszyk[6], Sushil Kumar[2,7], Derrick Deming[2], Nienke Moret[5], Steven Rodriguez[5], Kartik Subramanian[5], Meri Rogava[3,4,5], Adam N.R. Cartwright[2], Adrienne Luoma[2], Shaolin Mei[5], Titus J. Brinker[8,9], David M. Miller[10], Alexander Spektor[11], Dirk Schadendorf[12], Nicolo Riggi[6], Kai W. Wucherpfennig[2,7], Peter K. Sorger[5,13], and Benjamin Izar[1,2,3,4,5,13,14]

ABSTRACT

Patients with melanoma resistant to RAF/MEK inhibitors (RMi) are frequently resistant to other therapies, such as immune checkpoint inhibitors (ICI), and individuals succumb to their disease. New drugs that control tumor growth and favorably modulate the immune environment are therefore needed. We report that the small-molecule CX-6258 has potent activity against both RMi-sensitive (RMS) and -resistant (RMR) melanoma cell lines. Haspin kinase (HASPIN) was identified as a target of CX-6258. HASPIN inhibition resulted in reduced proliferation, frequent formation of micronuclei, recruitment of cGAS, and activation of the cyclic GMP-AMP synthase (cGAS)–stimulator of interferon genes (STING) pathway. In murine models, CX-6258 induced a potent cGAS-dependent type-I IFN response in tumor cells, increased IFNγ-producing CD8^{+} T cells, and reduced Treg frequency *in vivo*. HASPIN was more strongly expressed in malignant com- pared with healthy tissue and its inhibition by CX-6258 had minimal toxicity in *ex vivo*–expanded human tumor-infiltrating lymphocytes (TIL), proliferating TILs, and *in vitro* differentiated neurons, suggesting a potential therapeutic index for anticancer therapy. Furthermore, the activity of CX-6258 was validated in several Ewing sarcoma and multiple myeloma cell lines. Thus, HASPIN inhibition may overcome drug resistance in melanoma, modulate the immune environment, and target a vulnerability in different cancer lineages.

Significance: HASPIN inhibition by CX-6258 is a novel and potent strategy for RAF/MEK inhibitor–resistant melanoma and potentially other tumor types. HASPIN inhibition has direct antitumor activity and induces a favorable immune microenvi-ronment.

Introduction

The therapeutic options for patients with advanced or metastatic melanoma have significantly improved in the last decade. About half of melanomas harbor *BRAF* mutations, which sensitizes tumors to RAF/ MEK inhibitors (1–5). A major limitation of these drugs is intrinsic and acquired resistance (6). For patients who respond initially and then exhibit RAF/MEK inhibitor resistance (RMR), disease pro-gression is often rapid with reduced responsiveness to subsequent therapies, including immune checkpoint inhibitors (ICI), such as anti-CTLA-4 and/or anti-PD-1/PD-L1 (7, 8). In contrast to a 40%– 60% (9, 10) response rate in the first-line setting, ICI therapy is effective in only 0%–12% of RMR patients. The reasons for this observation are poorly understood at a molecular level, but it is plausible that rapid tumor growth in RMR patients outpaces the relatively slow pharmacodynamics of ICI, so that patients die before experiencing the benefits of ICIs. It seems possible that this challenge will also impact the treatment of other tumor types in which oncogene-targeted and ICI therapies are currently alternative possibilities. New drugs able to control tumor outgrowth and increase the likelihood of response to ICI by inducing a favorable immune environment could therefore be beneficial.

An emerging therapeutic strategy in the treatment of multiple types of cancer is the use of inhibitors of cell-cycle regulators, such as cyclin dependent kinases (CDK) and Aurora kinase, in conjunction with immunotherapy. CDK4/6 inhibitors, for example, enhance antitumor immunity by increasing responsiveness to ICIs and/or by activation of NK cells (11, 12). PARP and Aurora kinase inhibitors activate the DNA damage response machinery and may trigger cytosolic DNA sensing via cyclic GMP-AMP synthase (cGAS)–stimulator of interferon genes (STING), resulting in expression of type I IFN response (13). This may, in turn, promote an immunogenic tumor environment that is favor-able to immunotherapy. However, some of these agents, such as

[1]Department of Medical Oncology, Dana-Farber Cancer Institute, Boston, Mas-sachusetts. [2]Department of Cancer Immunology and Virology, Dana-Farber Cancer Institute, Boston, Massachusetts. [3]Columbia University Medical Center, Division of Hematology and Oncology, New York, New York. [4]Columbia Center for Translational Immunology, New York, New York. [5]Laboratory for Systems Pharmacology, Harvard Medical School, Boston, Massachusetts. [6]Experimental Pathology Service, Centre Hospitalier Universitaire Vaudois, University of Lau-sanne, Lausanne, Switzerland. [7]Department of Immunology, Harvard Medical School, Boston, Massachusetts. [8]National Center for Tumor Diseases (NCT), German Cancer Research Center (DKFZ), Heidelberg, Germany. [9]Department of Dermatology, University Hospital Heidelberg, Heidelberg, Germany. [10]Depart-ment of Dermatology, Massachusetts General Hospital, Boston, Massachusetts. [11]Department of Radiation Oncology, Dana-Farber Cancer Institute, Boston, Massachusetts. [12]Department of Dermatology, University Hospital Essen and German Cancer Consortium (DKTK), Essen, Germany. [13]Ludwig Center for Cancer Research at Harvard, Boston, Massachusetts. [14]Broad Institute of MIT and Harvard, Cambridge, Massachusetts.

Note: Supplementary data for this article are available at Cancer Research Online (http://cancerres.aacrjournals.org/).

Corresponding Author: Benjamin Izar, Columbia University Medical Center, 1790 Broadway, New York, NY 10019. Phone: 212-304-5871; E-mail: Bi2175@cumc.columbia.edu

Aurora kinase inhibitors, have significant off-target activity and their clinical use may be limited by toxicity (14).

In this study, we identify a small-molecule (CX-6258) that overcomes resistance to RAF/MEK inhibitors in melanoma cell lines. CX-6258 is annotated as an inhibitor of the PIM kinase family (15), but we find that it is primarily a potent inhibitor of the Histone H3–associated protein serine/threonine kinase (HASPIN), an understudied kinase (16). HASPIN, but not PIM1-3 inhibition, triggers a cascade of DNA damage, micronuclei formation, and activation of cGAS–STING, resulting in type I IFN expression in tumor cells. As a result, the immune microenvironment is depleted of immunosuppressive T-regulatory cells and there is an increase in IFNγ-producing $CD8^+$ T cells. We find that HASPIN inhibition is a vulnerability in other cancers, including multiple myeloma and Ewing sarcoma, and we demonstrate activity of CX-6258 in these settings. We propose that HASPIN inhibition may be a feasible therapeutic strategy in RMR melanoma and other tumor lineages by mediating antitumor activity through both cell-intrinsic mechanisms and modulation of the immune microenvironment.

Materials and Methods

Cell lines

A375 were cultured in DMEM (Gibco Life Technologies) supplemented with 10% FBS (Gibco). UACC62 were cultured in RPMI1640 with 10% FBS. Braf/Mek inhibitor–resistant cell lines were generated by culturing Braf/Mek inhibitor–sensitive cell lines in 10 nmol/L dabrafenib and 1 nmol/L trametinib (A375) or 7.5 nmol/L dabrafenib and 0.75 nmol/L trametinib (UACC62) until resistant clones emerged.

The murine cancer cell line CT26 was from ATCC and was cultured in RPMI1640 with 10% FBS.

Human myeloma cell lines AMO1, NCI-H929, SK-MM-1, U266, JJN3, and KMS-12-BM were purchased from DSMZ. KMS-20 cells were kindly provided by Dr. K.C. Anderson (Dana-Farber Cancer Institute, Boston, MA). These cells were cultured in RPMI1640 medium supplemented with 10% FBS (Lonza) and 1% penicillin/streptomycin. The IL6-dependent cell line XG-1, kindly provided by Dr. Renate Burger (University of Erlangen-Nuremberg, Erlangen, Germany), was cultured in the presence of 2.5 ng/mL rhIL6 (R&D Systems). Ewing sarcoma cell lines RDES, SK-ES-1, and SK-NEP-1 were obtained from ATCC. SK-ES-1 and SK-NEP-1 cells were cultured in McCoy 5A–modified medium (Gibco), supplemented with 15% FBS (PAN-Biotech). RDES cells were cultured in RPMI1640 medium 10% FBS.

Cells were short tandem repeat authenticated. All cell lines were grown at 37°C, 5% CO_2 in antibiotic-free media and repeatedly tested negative for *Mycoplasma* using PlasmoTest (InvivoGen).

ATP assay

Melanoma cells were seeded at 2×10^4 cells per well of a 96-well plate, allowed to adhere overnight, and then treated with 1 μmol/L (screen) or a dilution series of the drugs indicated, with 6 wells per concentration/condition. Seventy-two to 96 hours after drug treatment, half of the cell culture media was removed and 50 μL of Cell Titer-Glo (CTG) assay reagent (Promega) was added. Luminescence was detected after 10-minute incubation on a PerkinElmer Envision Plate reader (PerkinElmer).

Human myeloma cell lines were cultured in suspension using 12-well plates (10^5 cells/well; final volume 2 mL) in the presence of CX-6258 or DMSO as control. After 72 hours, cell viability was evaluated by CTG. For CTG assay, 50 μL from each experimental point were

plated in triplicates in 96-well plates; then, 50 μL of CTG was added and luminescence was detected by SpectraMax M3 (VWR), according to the manufacturer's instructions.

To perform viability assay on Ewing sarcoma cell lines, RDES and SK-ES-1 cells were seeded at a density of 15,000 cells per well, and SK-NEP-1 at a density of 5,000 cells per well, in 4 replicates in black opaque 96-well plates, with complete medium containing either the drug or an equal volume of solvent (DMSO). After 96 hours, CTG was added and luminescence was measured with a SynergyMx instrument (BioTek). All values are reported as percent of the signal obtained with control cells treated with DMSO only. Dose–response curves were fitted to the data using GraphPad Prism 8.0 (GraphPad) using a nonlinear fit with variable slope (four parameters).

In vitro measurement of kinase-inhibitory activity

CX-6258 was assayed using the KINOMEscan assay platform (DiscoverX). Data are reported as percent of remaining activity at 100 nmol/L drug concentration. The activity of CX-6258, SGI-1776, AZD1208, and PIM-447 on PIM1, PIM2, PIM3, Haspin, and MYLK4 were assayed using Reaction Biology Corporation's Kinase Profiling services as described previously (17). IC_{50} values were obtained from 10-point dose curves (3-fold dilutions with a maximum concentration of 1 μmol/L). An ATP concentration of 10 μmol/L was used. All compounds were obtained from Selleckchem and tested for identity and purity by LC/MS inhouse as described in detail in the drug collection section of the HMS LINCS Database (http://lincs.hms.harvard.edu/db/sm/).

Measurement of cell viability and cell-cycle perturbation

Cells were seeded and treated as indicated above. Cells were stained and fixed for analysis at the time of drug delivery and after 48–96 hours of incubation roughly equivalent to two doubling times of each cell line. Cells were pulsed for 1 hour with EdU (Lumiprobe) and stained with 1:2,000 LIVE/DEAD Far Red Dead Cell Stain (LDR; Thermo Fisher Scientific), fixed with 3.7% formaldehyde for 30 minutes, and permeabilized with 0.5% Triton X-100 in PBS. The EdU was labeled with cy3-azide for 30 minutes. The cells were then blocked for 1 hour with Odyssey blocking buffer, and stained overnight at 4°C with 2 μg/mL Hoechst 33342 and a 1:1,000 dilution of anti-phospho-histone H3 (pHH3) Alexa 488 (Ser10, clone D2C8) conjugated antibody (Cell Signaling Technology) and imaged using a 10× objective on an Operetta microscope (PerkinElmer) and analyzed using Columbus software (PerkinElmer). DNA content, defined by the total Hoechst intensity within the nuclear mask, was used to identify cells in the G_1 and G_2 phases of the cell cycle. The average LDR, EdU, and phospho-histone H3 intensities within the nuclear masks were determined. The LDR signal was used to classify cells as live or dead, the EdU and pHH3 signals to identify S- and M-phase cells, respectively. Cells with intermediate DNA content and no EdU signal were classified as S-phase dropout cells. Live cell counts were normalized to DMSO-treated controls on the same plates to yield normalized growth rate inhibition (GR) values as described previously (18).

Live-cell cell-cycle imaging

A375 reporter cells stably expressing H2B-Venus and mCherry-geminin (1–110) were imaged as described previously (19). Details are described in Supplementary Data.

CRISPR/Cas9–mediated genome editing

Recombinant Cas9 protein (Makrolab) complexed with crRNA (Integrated DNA Technologies) was introduced into the tumor cell

lines by electroporation using Program FF-120 with SF-Buffer on an Amaxa 4D-Nucleofector (Lonza). The guide RNA sequences were: PIM1 [AGAAGGACCGGATTTCCGAC], PIM2 [CACTCGAAGTCGCACTGCTA], MYLK4 [GTGGTCAAACGCCGACCTGA], and Cgas [GCGAGGGTCCAGGAAGGAAC]. A guide targeting LacZ [GCTGAGCGCTCGGAGCGCCT] served as control.

Small interfering RNA–mediated gene knockdown

Previously validated small interfering RNA (siRNA) targeting Haspin (Ambion Silencer Select ID 38320 and 38321, Thermo Fisher Scientific) or negative controls were transfected into A375 cells using Lipofectamine RNAiMax Transfection Reagent (Thermo Fisher Scientific) using the manufacturer's recommended protocols.

Western blotting

Cell culture pellets were collected by scraping down the cells into ice-cold PBS. After centrifugation, pellets were either stored at $-20°C$ until further processing or immediately lysed using RIPA Buffer (Sigma-Aldrich) supplemented with Halt Protease and Phosphatase Inhibitor Cocktail for 30 minutes on ice. Samples were then microcentrifuged at $12,000 \times g$ to remove debris. Protein concentration of the lysate was estimated using BCA assay using Pierce BCA Protein Assay Kit (Thermo Fisher Scientific). Equal amounts of protein were boiled with $6\times$ SDS-sample Buffer (Boston BioProducts) for 10 minutes and loaded on 10% TGX stain-free FastCast Acrylamide gels (Bio-Rad). Protein was transferred to polyvinylidene difluoride membranes, blocked for 1 hour at room temperature with 5% milk in TBS-T and the membranes were probed with primary antibodies in 5% BSA overnight. Primary antibodies were procured from the following manufacturers: PIM-1 (D8D7Y); PIM-2 (DID2); PIM-3 (D17C9); phospho-BAD (Ser 112) (40A9); CHK2 (D9C6); phospho-CHK2 (Thr68) (C13C1); p53 (1C12); phospho-p53 (Ser 392); STING (D1V5L); phospho-STING (Ser 365) (D8F4W); CGAS (D1D3G), (D3O8O); MEK-1/2; phospho- MEK-1/2 (Ser 217/221); ERK1/2 (3A7); phospho- ERK1/2 (Thr202/Tyr204), and Vinculin (Cell Signaling Technology Inc.). Haspin (ab226222) was obtained from Abcam. After washing, the membranes were probed with anti-rabbit IgG and anti-mouse IgG horseradish peroxidase–linked secondary antibodies (Cell Signaling Technology) and imaged on a LI-COR Odyssey Fc Imaging System. Equal protein loading was assessed using actin or vinculin antibodies and fluorescent detection.

qPCR

Total RNA was isolated using RNeasy Plus Kit (Qiagen) and 500 ng RNA per 20 μL reaction was transcribed into cDNA using iScript Supermix (Bio-Rad). TaqMan assays (Thermo Fisher Scientific) for Ifna1 (#Mm00439552_s1) and Ifnb1 (#Mm03030145_gH) were run on a QuantStudio 6 Flex (Applied Biosystems) with TaqMan gene expression MasterMix (Thermo Fisher Scientific). Gapdh (Mm99999915_g1) and Actb (Mm00607939_s1) were used as reference genes for normalization. All expression values were calculated using $\Delta\Delta C_t$ and are reported as relative expression values.

Immunofluorescence

For immunofluorescence studies, cells were grown on black walled 96-well plates (Corning) and treated as indicated. For staining of phosphor-H2A.X, centromeres (CREST), tubulin, or cGAS cells were fixed and permeabilized as described above. After blocking for 1 hour at room temperature with Odyssey blocking buffer (LI-COR) cells were stained overnight at 4°C with a 1:400 dilution of rabbit anti-phospho-H2AX.X S139 (9718, Cell Signaling Technology), or a 1:1,000 dilution of human anti-CREST (HCT-0100, ImmunoVision) and a 1:400 dilution of rabbit anti-β-tubulin (2128, Cell Signaling Technology), or a 1:200 dilution of rabbit anti-cGAS antibody (D1D3G, Cell Signaling Technology). After washing, cells were stained with secondary anti-Rabbit Alexa-488 or anti-human Alexa-647 (Thermo Fisher Scientific). After washing, nuclei were stained using 2 μg/mL Hoechst 33342 (Sigma Aldrich) for 1 hour at room temperature.

Representative images were taken with an Olympus IX72 (Olympus) equipped with a 20× objective and Orca Spark camera (Hamamatsu) operated with CellSens software or selected from plate scans with a GE IN Cell Analyzer 6000 (GE Healthcare). For quantification purposes, plates were scanned using a GE IN Cell Analyzer 6000 and cGas spots, micronuclei, and γH2AX spots were quantified from five random fields per well using the Columbus image data storage and analysis system (PerkinElmer).

Animal experiments

All animals used were ordered from Jackson Laboratory. Tumor size was measured at least twice per week using a digital caliper and tumor volume was calculated using the formula $V = (W^2 \times L)/2$, with W being the shorter and L being the longer diameter.

For A375 xenograft studies, 6-week-old female N:J mice were subcutaneously injected with 2.5×10^6 cells per mouse in a 1:1 PBS/Matrigel mixture. Treatment was administered by oral gavage when tumor became palpable and mice were treated for five days with 100 mg/kg body weight (bw) CX-6258 dissolved in water.

For CT26 studies in N:J mice, 3×10^5 cells per mouse were injected in PBS subcutaneously, and treatment was administered by oral gavage when tumors became palpable. Mice received treatment via oral gavage on five consecutive days with doses of either 10 mg/kg bw or 100 mg/kg bw CX-6258.

For syngeneic CT26 studies, 6- to 8-week-old female Balb/c mice were subcutaneously injected with 4×10^5 cells per mouse in PBS. On day 5 to 7, treatment was initiated when tumors were palpable. The CX-6258 only group received either 10 mg/kg bw or 100 mg/kg bw CX-6258 per oral gavage for three or four consecutive days, respectively. The anti-PD1 only group received three intraperitoneal injections of 200 μg anti-PD1-antibody (29F.1A12, InVivoMab, BioXcel) on days 5, 8, and 11 or 7, 10, and 13 as indicated in the respective experiment. The phased therapy group received anti-PD1 at the same days as the anti-PD1 only group, but received an additional three days of 10 mg/kg bw or four days of 100 mg/kg bw CX-6258 per oral gavage from day 8 or 10 onwards. Control animals received isotype control antibody. For survival analysis, endpoints were defined as >700 mm^3 tumor volume or central ulceration and necrosis. All animal studies were approved under animal protocol 08-049 at Dana-Farber Cancer Institute.

Immunophenotyping

To characterize the immune response in tumor-bearing mice from above experiment, mice were treated as described above. On day 16, mice were sacrificed and spleens, tumor draining lymph nodes (tdLN), and tumors were harvested, and single-cell suspensions were generated by mechanical and enzymatic digestion. Dead cells were labeled using Zombie NIR (BioLegend) in PBS for 15 minutes at room temperature. Thereafter, surface antigens were stained in PBS supplemented with 3% FBS and 2 mmol/L EDTA for 30 minutes on ice using anti-CD45-BV510 (30-F11, BioLegend), anti-CD3-PE-Cy5 (145-2C11, BioLegend), anti-CD4-BV605 (RM4-5, BioLegend), anti-CD8a-BV785 (53-6.7, BioLegend), anti-NKp46-PE (145-29A1.4, BioLegend),

anti-CD14-APC (Sa14.2, BioLegend), anti-CD45R-APC (RA3-6B2, BioLegend), and anti-F4/80-APC (BM8, BioLegend).

Cells were fixed using the eBioscience Foxp3/Transcription Factor Staining Buffer (Thermo Fisher Scientific) as recommended by the manufacturer. Intracellular FOXP3 was stained using anti-FOXP3-BV421 (MF-14, BioLegend). Ki67 was stained using anti-Ki67-FITC (SolA15, eBioscience).

For staining of intracellular IFNγ TILs isolated from tumors were seeded in 96-well round bottom plates in RPMI supplemented with 10% FBS, GlutaMax, 10 mmol/L HEPES, and 55 μmol/L β-Mercaptoethanol. Cells were stimulated for 4 hours in 37°C and 5% CO_2 using a combination of phorbol 12-myristate-13-acetate (PMA) and ionomycin (BioLegend) and washed once with PBS. Viability and surface antigens were stained as described above. Cells were fixed using the eBioscience Foxp3/Transcription Factor Staining Buffer (Thermo Fisher Scientific) and intracellular IFNγ was stained using anti-IFNγ-PerCp-Cy5.5 (XMG1.2, BioLegend)

Cells were acquired with a Sony SP6800 Spectral Flow Cytometer (Sony) and the data were analyzed using FlowJo 10.5.3 (TreeStar). Fluorescence minus one (FMO) gating controls were used for FOXP3, Ki67, and IFNγ.

Toxicity assessment in human tumor-infiltrating lymphocytes

Human tumor-infiltrating lymphocytes (TIL) from patients with melanoma were cultured and expanded as described previously (20). To assess cytotoxicity of CX-6258 on human TILs, cells were seeded in RPMI with 10% human AB serum, 3,000 IU/mL hIL2 at 1×10^5 cells per well of a 96-well round bottom plate (Corning), and treated with increasing doses of CX-6258 in triplicates. After 48 hours, cells were collected, washed once with PBS, and resuspended in Annexin V staining buffer. Cells were stained with Annexin V-FITC and propidium iodide (PI; Cell Signaling Technology) and analyzed on a Sony SP6800 Spectral Flow Cytometer. Data were analyzed using FlowJo 10.5.3 (TreeStar) and viable cells defined by negative staining for Annexin V and PI are reported. For proliferation assays, 5×10^4 TILs were stained with carboxyfluorescein diacetate succinimidyl ester (CFSE; Invitrogen) and seeded together with anti-CD3/CD28 Beads (Invitrogen) and increasing doses of CX-6258 in T-cell media supplemented with 30 IU/mL IL2. Cells were collected on days 1, 3, and 5, stained for viability using Zombie UV dye (BioLegend) and fixed using 4 % formaldehyde in PBS. Cells were analysed by FACS on a BD Fortessa (Becton Dickinson). Data analysis was performed with FlowJo 10.5.3 (TreeStar) and viable cells were defined by negative staining for Zombie and analyzed for CFSE intensity.

Statistical analysis

Statistical analysis was performed using GraphPad Prism 8 (GraphPad Software). For experiments with two groups, Student t test was used. For comparison of three or more groups, variance was assessed using ANOVA and significance was calculated using Tukey *post hoc* test correcting for multiple comparison and P_{adj} values are reported. Tumor growth curves were compared using two-way ANOVA or mixed effects analysis with Tukey *post hoc* test comparing treatment means. Survival was analyzed using a log-rank test. P values < 0.05 were considered significant.

Results

Inhibition of HASPIN shows activity in RAF/MEK inhibitor–sensitive and -resistant melanoma

To model RMR, we used two RMI-sensitive human $BRAF^{V600E}$ melanoma cell lines (A375-S and UACC62–S) and generated resistant lines (A375-RMR and UACC62-RMR) by continuous culture in the presence of the RAF inhibitor dabrafenib and MEK inhibitor trametinib (Supplementary Fig. S1A). As expected, ERK was inhibited in RMS lines in the presence of RAF/MEK inhibitors and active in RMR lines (as assayed by pERK levels); RMR cells grew at a similar rate to RMS cell lines and required significantly higher doses of dabrafenib or trametinib to inhibit proliferation (Supplementary Fig. S1B–S1G). We then screened a focused 14-member small-molecule library (Supplementary Table S1) consisting of compounds reported to inhibit proteins in the JAK/STAT pathway, a previously reported putative vulnerability in RMR (21). Both S and RMR cell lines were treated with 1 μmol/L drug for 3 days and viable cell numbers were inferred from ATP levels in cell extracts; by this measure, CX-6258 was highly active in both A375-S and A375-RMR cells, as well as UACC62-S and UACC62-RMR (**Fig. 1A** and **B**; Supplementary Fig. S1H; EC_{50} ~100 nmol/L in A375 and ~300 nmol/L in UACC62). When we corrected for differences in A375 and UACC62 proliferation rates using the normalized GR metric (18), CX-6258 was equally potent in both cell lines with $GR_{50} \sim 200$ nmol/L and $GR_{max} \sim 1$ μmol/L (**Fig. 1C** and **D**).

To assess activity *in vivo*, we generated xenografts of A375-S and A375-RMR in nude mice ($n = 5$/group) and treated animals for 5 days with either vehicle control or CX-6258 (100 mg/kg) by daily oral gavage. CX-6258 significantly reduced tumor growth in both types of tumor (A375-S vs. A375-S plus CX-6258; $P = 0.02$; A375-RMR vs. A375-RMR plus CX-6258, $P = 0.01$, by two-way ANOVA) demonstrating oral bioavailability (**Fig. 1E**). Nude mice treated with CX-6258 did not display weight loss, suggesting *in vivo* tolerability of the compound (Supplementary Fig. S1I).

To test the impact of CX-6258 on immune cells, we generated two independent cultures of patient-derived TILs by *ex vivo* expansion. We then treated TILs with increasing doses of CX-6258 and measured cell viability by flow cytometry using Annexin/PI staining. At the GR_{50} dose in melanoma cells of ~200 nmol/L, both TIL cultures had >98% viability (**Fig. 1F**); a significant reduction in viability was observed only at doses $> 15 \times GR_{50}$ (>3 μmol/L). To assess whether CX-6258 impairs proliferation of TILs, we stimulated human TILs with anti-CD3/CD28 beads in the presence of CX-6258. At concentrations effective in cancer cells, proliferation was not impaired (**Fig. 1G** and **H**; Supplementary Fig. S1J) suggesting a therapeutic window. To assess potential toxicity in other cell types, we treated *in vitro*–differentiated human neurons with CX-6258. Cell counts were not reduced in cells treated with CX-6258 at 100 nmol/L compared with DMSO-treated cells (mean difference 0.04%, $P_{adj} > 0.99$ ANOVA) while doses of 300 nmol/L to 10 μmol/L resulted in modest reduction of cell numbers (**Fig. 1I**). Thus, CX-6258 is active against melanoma cells and modestly toxic against human TILs and neurons *in vitro*.

CX-6258 acts as a HASPIN inhibitor

CX-6258 is annotated as an inhibitor of PIM kinases (15), a family of kinases that act downstream of the JAK/STAT pathway. As kinase inhibitors frequently exhibit target promiscuity, we aimed to identify kinase targets bound by this small molecule in an unbiased fashion and we used the KINOMEscan assay (DiscoverX) to determine its affinity for 468 human kinases. As described previously, CX-6258 bound PIM1—3, but also bound MYLK4 and HASPIN with high affinity (**Fig. 1J**; Supplementary Fig. S1K). When we compared CX-6258 to three related compounds (AZD1206, PIM447, and SGI-1776) using *in vitro* kinase assays, we observed IC_{50} values ranging from pico- to
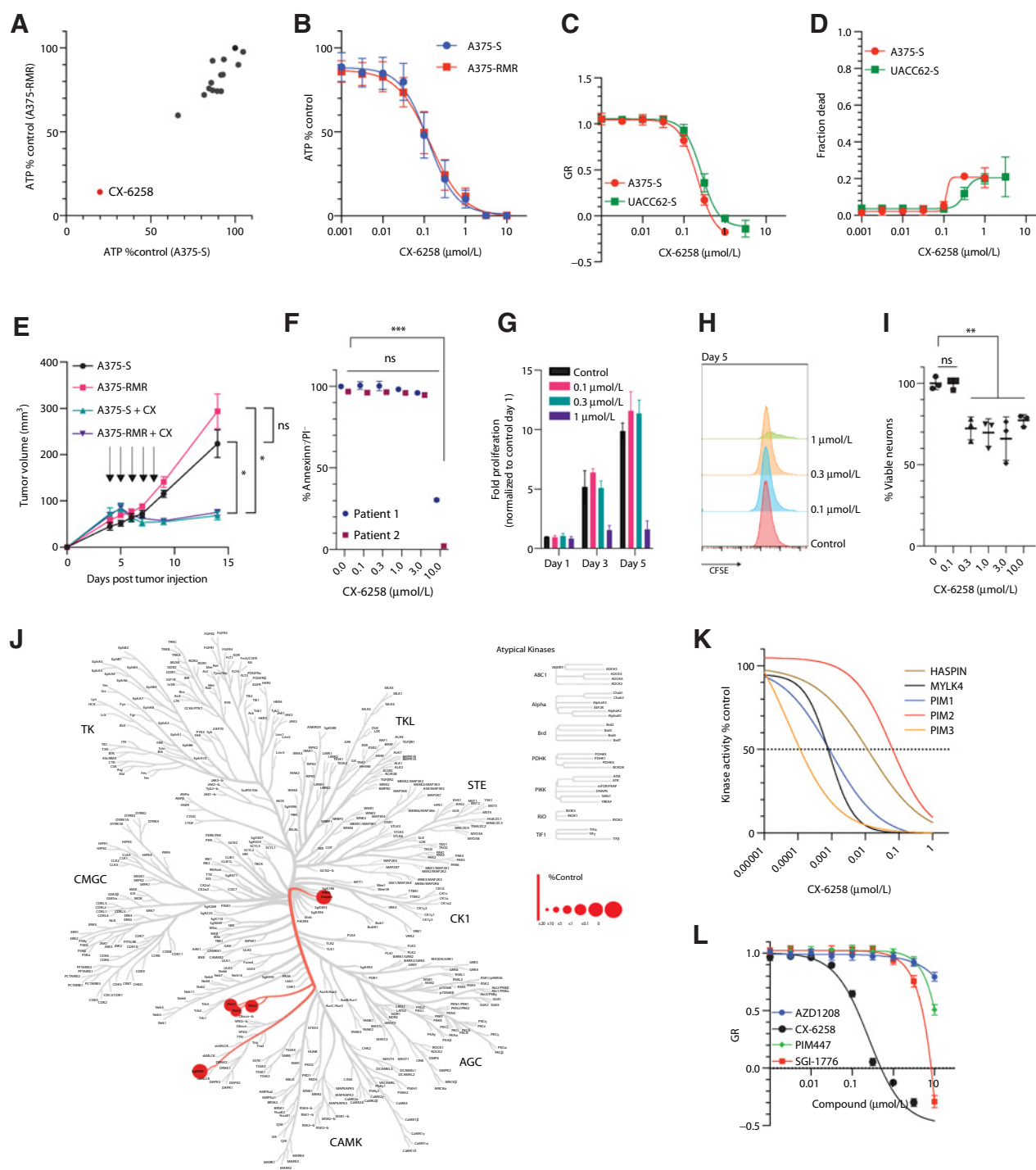
Melms et al.

Figure 1.

A, Summary of drug screen. Relative viability of melanoma cell lines A375-S (sensitive to RAF/MEK inhibitors) and A375-RMR (resistant to RAF/MEK-inhibitors) treated with a focused drug library (Supplementary Table S1). The x-axis indicates the percent viability of A375-S treated with the drug library compared with DMSO treatment; y-axis indicates the percent viability of A375-RMR treated with the drug library compared with DMSO treatment. Each compound in the library is indicated by a dot with a different color. CX-6258 is labeled separately. **B,** Dose–response curve of A375-S and A375-RMR. CX-6258 was given at doses indicated in x-axis and viability was measured using ATP. The y-axis indicates percent viability of CX-6258–treated cells versus DMSO-treated cells. **C** and **D,** GR-corrected effect of CX-6258 at different doses; x-axis indicates concentration (μmol/L) of CX-6258 and y-axis indicates GR response of A375-S and UACC52-S (**C**) and fraction of dead cells with y-axis indicating fraction of dead cells compared with vehicle-treated cells (**D**). **E,** Nude mice ($n = 5$/group) were injected with A375-S or A375-RMR and treated with either CX-6258 or vehicle at days indicated by arrows. x-axis indicates days since tumor injection; y-axis indicates tumor volume (in mm^3). Animals treated with CX-6258 had significantly smaller tumors compared with vehicle-treated animals ($n = 5$/group; error bars, mean $\pm$ SEM; A375-S vs. *(Continued on the following page.)*

nanomolar for PIM1/2/3, MYLK4, or HASPIN (**Fig. 1K**; Supplementary Fig. S1L–S1O). Despite having partially overlapping target spectra, GR_{50} values for AZD1206, PIM447, and SGI-1776 in A375 were approximately 30-fold higher (>3 μmol/L) than CX-6258 (**Fig. 1L**) demonstrating that CX-6258 has higher activity in cell-based assays.

To investigate the relevance of CX-6258 targets for its biological activity we generated a series of CRISPR-Cas9 knockouts (KO) of PIM1, PIM2, and MYLK4; knockdown was confirmed by Western blot analysis (for PIM) or qPCR (for MYLK4, reduced expression −77.9%, $P = 0.0154$, t test), respectively (**Fig. 2A** and **B**). As compared with control lines electroporated with a nontargeting guide RNA (LacZ), there was no significant difference in proliferation rates for cells with KO in PIM1 (relative proliferation rate = 0.8, $P_{adj} = 0.08$, one-way ANOVA), PIM2 (relative proliferation rate = 1.1, $P_{adj} = 0.47$, one-way ANOVA), or MYLK4 (relative proliferation rate = 1; **Fig. 2C** and **D**). We were unable to establish a KO for PIM3. Furthermore, none of these KOs altered GR values for CX-6258, suggesting that PIM kinases and MYLK4 are not the relevant cellular targets of CX-6258 in melanoma cells (**Fig. 2E** and **F**). Consistent with a PIM kinase–independent mode of action, exposure of cells to CX-6258 did not reduce the levels of BAD phosphorylation, a known downstream target of PIM kinases, suggesting that PIMs are not the cellular target of CX-6258 or that other pathways compensate for the loss of PIM activity in melanoma cells (**Fig. 2G**).

To investigate possible off-target activities of CX-6258 on pathways known to be important for the proliferation of melanoma cells, we used Western blotting against activating phosphorylation sites on proteins in the RAF-MEK-ERK, AKT, and JAK/STAT pathways before and after treatment of cell lines to CX-6258. We observed no significant differences in A375-S and A375-RMR at drug concentrations as high as 1 μmol/L (**Fig. 2H**). In a complementary experiment, we overexpressed wild-type or kinase-dead PIM kinases (PIM-1-KD, PIM-2-KD, PIM-3-KD) (**Fig. 2I**) in A375-S cell lines and observed no change in proliferation rates as compared with EGFP-transduced control cells ($P = 0.56$ and $P = 0.47$, one-way ANOVA; **Fig. 2J** and **K**). These data suggest that neither PIM kinases and MYLK4, nor components of signal transduction pathways required for the growth of melanoma cells are responsible for the antiproliferative effects of CX-6258. We hypothesize that these effects are mediated by inhibition of HASPIN.

The only well-described function of HASPIN is phosphorylation of Histone 3 (H3) on threonine 3 (H3pT3), which promotes binding of the chromosomal passenger complex (CPC) and regulates progression through mitosis (22). Treatment of melanoma cells lines with CX-6258 reduced H3pT3 in a dose-dependent fashion ($EC_{50} \sim 150$ nmol/L; **Fig. 2L**; Supplementary Fig. S2A). In addition, transfection of A375-S with previously validated siRNA against HASPIN (Supplementary Fig. S2B) resulted in significant reduction in cell numbers as compared with a nontargeting siRNA (−63.86%, $P < 0.0001$, t test; **Fig. 2M**).

Together, these results suggest that HASPIN is a key cellular target of CX-6258 and responsible for its antitumor activity, while preserving viability of human TILs and neurons.

On-target inhibition of HASPIN results in reduced proliferation and increased formation of micronuclei

To study the effects of CX-6258 on cell division, we performed EdU incorporation assays and found that CX-6258 caused dose-dependent arrest in G_2–M in A375 and UACC62 cells (**Fig. 3A** and **B**; Supplementary Fig. S3A). At higher drug doses, we identified cells with DNA content >4N. This has previously been reported in cells treated with Aurora kinase inhibitors further supporting CX-6258 acting at the level of CPC recruitment and function (23). These observations were also true in the murine cancer cell line CT26 that was used for the syngeneic mouse studies described below, although we observed a larger number of cells with a DNA content >4N and reduced GR_{max} compared with human melanoma cell lines (Supplementary Fig. S3B and S3C).

To study mitotic progression, parental A375 cells were transduced with a dual-reporter system (geminin-mCherry and H2B-YFP) followed by live-cell fluorescence microscopy (19). Geminin accumulates during S/G_2 and M phases of the cell cycle and is rapidly degraded by the anaphase promoting complex at the metaphase to anaphase transition; the levels of geminin therefore identify cell-cycle stages. Expression of H2B-YFP reveals chromatin morphology and assists with cell tracking. We tracked a total of 307 cells in three conditions for 48 hours (DMSO, $n = 100$; 100 nmol/L CX-6258, $n = 102$; 300 nmol/L CX-6258, $n = 105$). In DMSO-treated cells, cells divided (on average) three times (**Fig. 3C**). Treatment with CX-6258 reduced the number of cell divisions in a dose-dependent manner (**Fig. 3C**; Supplementary Fig. S3D). A subset of cells failed to undergo chromosome condensation, segregation, and cytokinesis but still progressed through the cell cycle, as shown by changes in geminin intensity (i.e., cell #12 in the 0.1 μmol/L treatment group and cell #20 in the 0.3 μmol/L treatment group; **Fig. 3C**). Cells that progressed through mitosis exhibited mitotic mis-segregation as scored by chromosomal bridges during anaphase and formation of micronuclei in daughter cells (Supplementary Fig. S3E–S3G; Supplementary Video S1 and S2). Treatment with either 0.1 μmol/L or 0.3 μmol/L CX-6258 led to a significant accumulation of cells with postmitotic micronuclei after 48 hours (8.274% vs. 50.9% for DMSO vs. 0.1 μmol/L, P_{adj} 0.01; 8.274 % vs. 57.8% for DMSO vs. 0.3 μmol/L, $P = 0.005$; one-way ANOVA; **Fig. 3D**). In CX-6258–treated cells, micronuclei costained with CREST, a marker for centromeres, suggesting that micronuclei were composed of chromosomes fragmented by abnormal mitotic segregation and supporting a function for HASPIN in mitosis (**Fig. 3E**). To investigate the acute loss of HASPIN on mitotic progression, we treated A375-S with previously validated siRNA against HASPIN (Supplementary Fig. S2B). This resulted in lagging chromosomes,

---

(*Continued.*) A375-S + CX-6258, $P = 0.02$; A375-RMR vs. A375-RMR + CX-6258, $P = 0.01$; two-way ANOVA). **F,** Annexin/PI staining of two human *ex vivo*–expanded TILs from melanoma patient 1 and patient 2 treated with DMSO or increasing doses of CX-6258 as indicated on the x-axis; y-axis shows the percent of cells that are negative for both Annexin and PI (error bars, mean ± SD; ***, adjusted $P < 0.001$, ANOVA). **G,** Proliferation of *ex vivo*–expanded human TILs stimulated with CD3/CD28 in the presence of increasing doses of CX-6258. x-axis, days after stimulation; y-axis, fold expansion relative to control cells on day 1. Mean ± SD. **H,** Histograms of CFSE intensity dilution on day 5 of TILs compared with CFSE intensity on day 1; x-axis indicates CFSE intensity. **I,** Human *in vitro* differentiated neurons were treated with CX-6258 at doses indicated on x-axis; y-axis indicates relative cell counts. Error bars, mean ± SD. DMSO versus 0.1 μmol/L, $P_{adj} > 0.99$; DMSO versus 0.3–10 μmol/L, $P_{adj} = 0.03$–0.001, ANOVA). **J,** Human kinome screen for CX-6258. The tree represents different families of human kinases. Red circles indicate kinases that are bound by CX-6258. The size of the circles indicates the binding of the compound relative to controls. **K,** Dose–response inhibition for indicated targets by CX-6258 *in vitro*; x-axis indicates molarity of CX-6258 and y-axis indicates kinase activity *in vitro*. The dotted line represents IC_{50}. **L,** GR dose response in A375-S testing three functionally related compounds AZD1206, PIM447, and SGI-1776 compared with CX-6258; x-axis indicates doses in μmol/L and y-axis indicates GR response. **, $P < 0.01$; ***, $P < 0.001$; ns, nonsignificant.

Melms et al.
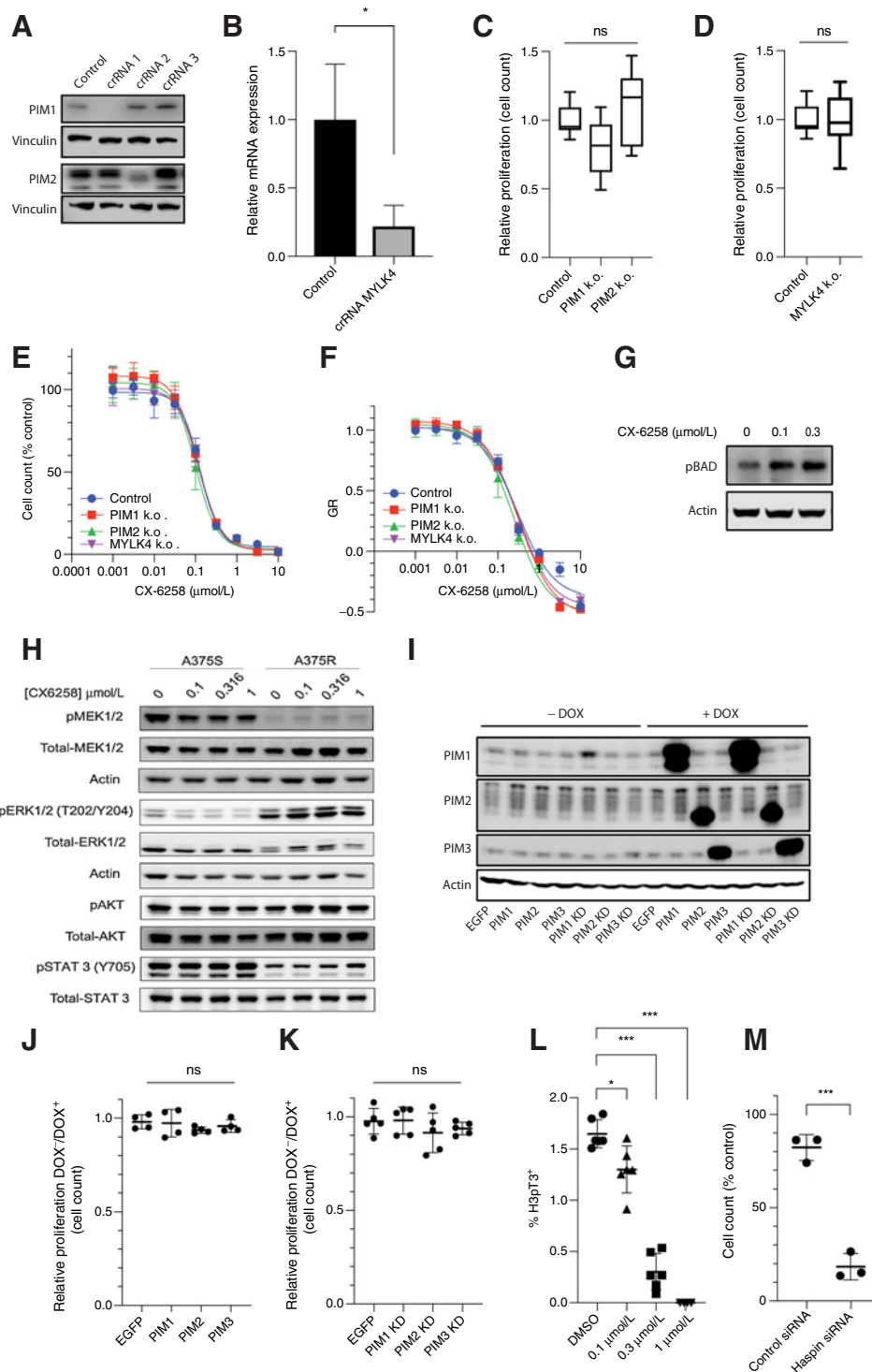
Figure 2.
A, Western blots of PIM-1 and PIM-2 CRISPR-Cas9 KO. Cells were electroporated with ribonucleotides of Cas9 protein with indicated crRNAs or LacZ controls. **B,** Relative mRNA expression of MYLK4 (y-axis) in isogenic A375-S MYLK4 CRISPR-Cas9 KO versus LacZ ($P = 0.0154$, t test). **C** and **D,** Proliferation rate of PIM-1-KO and PIM-2-KO, and MYLK4-KO from **A** and **B** compared with their isogenic LacZ control cell lines (PIM1KO relative proliferation rate $= 0.799$, $P_{adj} = 0.08$ one-way ANOVA; PIM-2KO relative proliferation rate $= 1.10$, $P_{adj} = 0.47$, one-way ANOVA). **E,** Dose response of PIM-1-KO, PIM-2-KO, and MYLK4-KO cell lines from **A** and **B** to CX-6258 at doses (x-axis, molarity) and in LacZ controls, with y-axis indicating percent cell number of CX-6258–treated cells compared with DMSO-treated cells. **F,** GR$_{50}$ in response to CX-6258 (x-axis, molarity) for all cell lines shown in **E**. The y-axis indicates growth rate inhibition. **G,** Western blot of phosphorylated BAD (pBAD) and actin loading control in A375S cell lines treated with CX-6258 at indicated doses. (*Continued on the following page.*)

formation of micronuclei, and reduction in proliferation (**Figs. 3F and 2M**), phenocopying the effects of CX-6258. In contrast, neither reduced proliferation nor increased formation of micronuclei was observed in cells with PIM1/2 or MYLK4 CRISPR-Cas9 KO. These data support that on-target inhibition of HASPIN by CX-6258 leads to mitotic errors, resulting in the generation of micronuclei.

Exposure of parental A375 cells to CX-6258 resulted in significant increases in phosphorylated H2A.X^{S139} (γH2AX) foci (DMSO vs. 0.1 μmol/L, 0.31 vs. 1.09 average number of foci per nucleus, $P_{adj} = 0.04$; DMSO vs. 0.3 μmol/L, 0.31 vs. 3.94, $P_{adj} < 0.001$, one-way ANOVA). γH2AX foci are a marker of double-stranded DNA breaks. At 0.1 μmol/L CX-6258, γH2AX staining was predominantly restricted to micronuclei, consistent with their origin in fragmented chromosomes, but at higher doses (0.3 μmol/L), the drug-induced multifocal γH2AX staining in the nucleus indicative of double-stranded DNA breaks throughout the genome (**Fig. 3G**; Supplementary Fig. S3H and S3I). This triggered the DNA damage response (DDR), as shown by increased phosphorylation of CHEK2 and increased abundance and phosphorylation of p53 (**Fig. 3H**). We conclude that inhibition of HASPIN results in DNA damage and the formation of micronuclei that are prone to rupture.

HASPIN inhibition induces type I IFN response in a cGAS-dependent fashion and reduced tumor growth *in vivo*

Formation and rupture of micronuclei has previously been shown to trigger the cytosolic DNA-sensor cGAS (24). UACC62 cells are cGAS-proficient (Supplementary Fig. S3J) and we found that exposure of these cells to CX-6258 at concentrations that still allowed cell division ($\sim$0.3 $\times$ GR$_{max}$; 0.3 μmol/L) triggered micronuclei formation (DMSO vs. 0.3 μmol/L, $P_{adj} < 0.0001$, ANOVA) and resulted in recruitment of cGAS specifically to micronuclei (**Fig. 3I–K**; Supplementary Fig. S3K). At drug concentrations high enough to fully block cell division (1 $\times$ GR$_{max}$ = 1 μmol/L), the frequency of micronuclei formation was lower and cGAS was not recruited (**Fig. 3K**). In addition, we observed increased levels and phosphorylation of STING, which is triggered by the cGAS product cGAMP, and induction of cGAS itself, consistent with a previously described positive feedback loop (**Fig. 3L**; ref. 25).

cGAS–STING pathway activation results in expression of antiviral immunity via type I IFNs (IFNα and IFNβ) and has potential benefits for antitumor immunity (26). To test for induction of a type I IFN response by CX-6258, we used CT26 murine cells, which are cGAS proficient and can be used to generate tumors in nude and immuno-competent mice. RT-PCR of CT26 cells exposed to CX-6258 at 0.1 μmol/L for five days revealed strong induction of mRNA for both IFNα1 (>60-fold, adjusted $P < 0.001$, ANOVA) and IFNβ1 (2.4-fold, $P_{adj} < 0.001$, ANOVA; **Fig. 3M and N**). To confirm that cGAS was necessary for IFN induction, we used CRISPR-Cas9 to knockout cGAS in CT26 cells (Supplementary Fig. S3L) and observed an approxi-mately 5-fold reduction in basal IFNβ1 levels ($P_{adj} < 0.001$, ANOVA) with no significant induction of IFNα and IFNβ by CX-6258 (**Fig. 3M and N**). Thus, CX-6258 triggers a type I IFN response in a cGAS-dependent manner.

To study the effects of CX-6258 *in vivo*, nude mice were engrafted with CT26 cells and treated with high and low doses of CX-6258 (10 and 100 mg/kg) for 5 days. Rates of tumor growth were variable ($n = 5$/group), but tumor volumes at day 14 were not significantly different in CX-6258–treated mice and vehicle-only controls (Supplementary Fig. S4A and S4B). The difference *in vivo* efficacy of CX-6258 in nude mice bearing A375 and CT26 tumors may reflect the fact that the drug is cytotoxic *in vitro* in A375, but not CT26 cells (**Fig. 1C**; Supplementary Fig. S3C). To see whether adaptive immunity might enhance the effects of CX-6258, CT26 cells were engrafted in immunocompetent BALB/c animals and cohorts of 8 animals were exposed to CX-6258, anti-PD-1 antibody, or a phased combination of CX-6258 plus anti-PD-1 (see study design in **Fig. 4A**). Animals treated with high-dose CX-6258 alone exhibited a significant reduction in tumor growth as compared with vehicle-only controls ($P_{adj} = 0.02$, two-way ANOVA); PD-1 alone did not reach statistical significance ($P_{adj} = 0.36$). Notably, the response to anti-PD-1 was variable and occurred in a delayed fashion. Phased combination of anti-PD-1 and CX-6258 led to a less variable and significant delay in tumor outgrowth ($P_{adj} < 0.002$, two-way ANOVA; **Fig. 4B and C**). The body weight of all treatment groups was higher compared with vehicle, and this was due to tumor outgrowth and associated effects in the vehicle control (Supplementary Fig. S4C). Thus, the antitumor activity of CX-6258 is substantially enhanced by the presence of an adaptive immune system, being substantially greater in immunocompetent than in nude mice. All treatment modalities significantly increased median survival compared with vehicle (Supplementary Fig. S4D) and phased combination delayed outgrowth compared with anti-PD-1, but did not provide an additional benefit in median survival over anti-PD-1 alone (vehicle vs. anti-PD-1, $P = 0.02$; vehicle vs. CX, $P = 0.04$; vehicle vs. phased, $P = 0.002$).

We hypothesized that response to CX-6258 (either alone or in phased combination with anti-PD-1 therapy) could be due to modulation of the tumor microenvironment (TME). To test this hypothesis, we treated animals with a similar treatment design (Supplementary Fig. S4E), but with a lower dose of CX-6258 (10 mg/kg), resulting in similar tumor volumes in all groups on day 15 after tumor implantation (Supplementary Fig. S4F). Tumors, tdLNs, and spleens were then harvested and subjected to analysis by flow cytometry ($n = 5$–6 animals per group; Supplementary Fig. S4G). The rate of proliferating immune cells, as assessed by Ki67 staining, was not different between treatment groups (Supplementary Fig. S4H). Compared with vehicle-only controls, CX-6258-alone increased infiltration of CD3$^+$ T lymphocytes into the TME (31% vs. 43%, $P_{adj} = 0.04$, ANOVA; Supplementary Fig. S4I). The most significant difference between treated and untreated animals was in the abundance of regulatory CD4$^+$ T cells (Tregs). Significant reduction in Tregs was observed in tumors treated with CX-6258 (30.57% vs. 18.8% of CD4$^+$, $P_{adj} = 0.008$, ANOVA) or anti-PD-1 therapy (30.57% vs. 19.63% of CD4$^+$, $P_{adj} = 0.01$, ANOVA)

(*Continued.*) **H,** Western blot analysis of total MEK1/2 and pMEK1/2, total ERK1/2 and pERK, total AKT and pAKT, and total STAT3 and pSTAT3, and actin controls in A375-S and A375-RMR following treatment with indicated doses of CX-6258. **I,** Western blots of PIM-1, PIM-2, and PIM-3 and actin loading controls in A375-S transduced with doxycycline-inducible vector for EGFP or ORFs for PIM-1, PIM-2, PIM-3, or kinase dead (KD) PIM-1-KD, PIM2-KD, or PIM3-KD with doxycycline ($+$Dox) or without ($-$Dox) doxycycline treatment. **J** and **K,** Proliferation rate of A375-S overexpressing PIM-1, PIM-2, or PIM-3 or matched KD cell lines compared with EGFP-overexpressing cells relative to parental controls with $+$Dox ($P = 0.56$ and 0.47, ANOVA). **L,** Frequency (in percent of all cells) of cells with positive Histone-3 phospho-threonine 3 (H3pT3) staining (*y*-axis) in A375-S cells treated with DMSO or indicated doses of CX-6258 showing a significant, dose-dependent reduction in response to CX-6258 treatment (error bars, mean $\pm$ SD, $P < 0.001$, linear trend significant, ANOVA). **M,** Fraction of cell numbers in percent of parental A375 cells (*y*-axis) following treatment with a nontargeting siRNA or HASPIN targeting siRNA 48 hours after transfection (error bars, mean $\pm$ SD; $P < 0.0001$, t test). *, $P < 0.05$; ***, $P < 0.001$; ns, nonsignificant.

Melms et al.
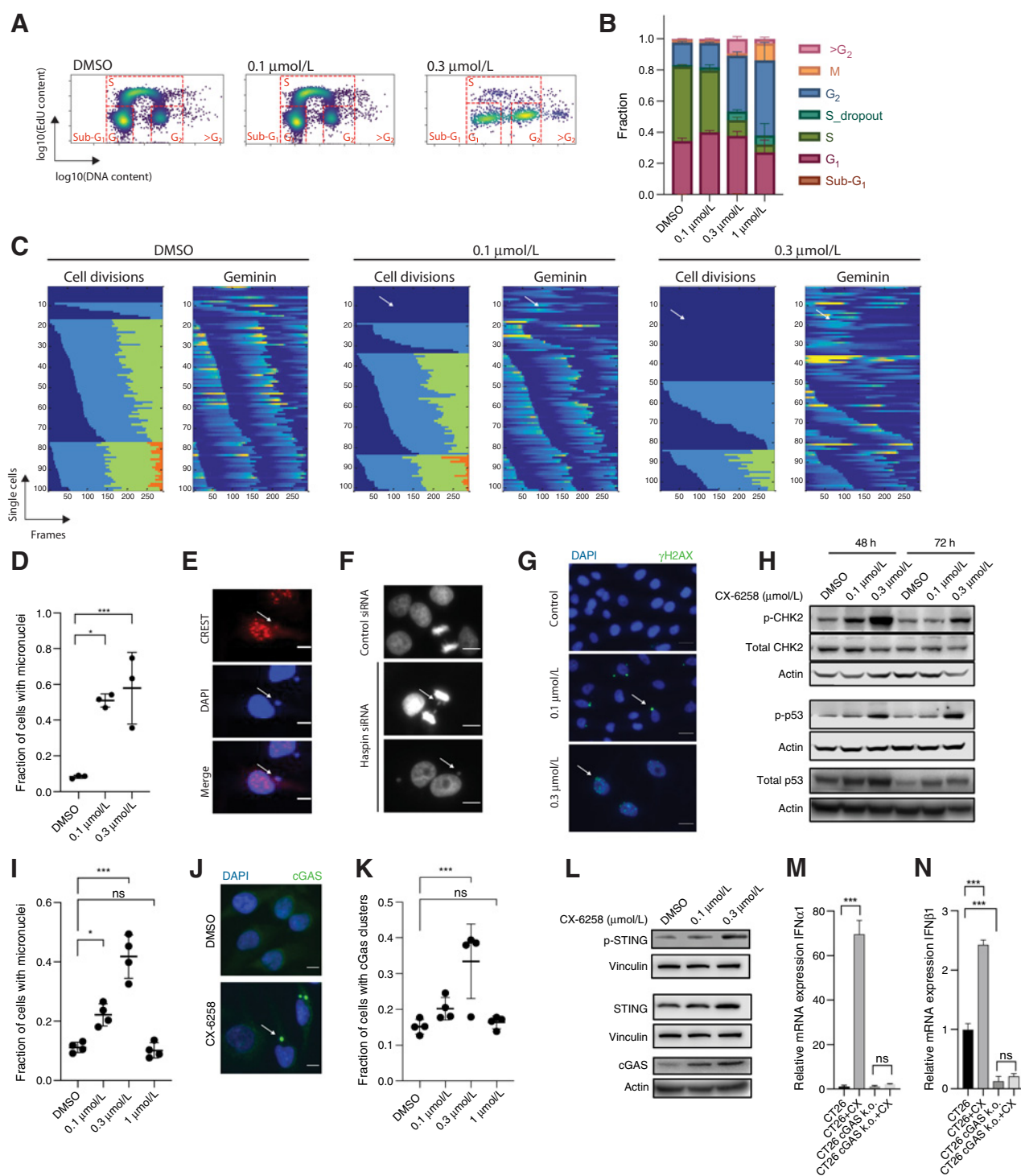
Figure 3.
A, EdU assay of A375S cells treated with DMSO or CX-6258 as indicated. x-axis indicates DNA content (log_{10}) and y-axis indicates EdU incorporation (log_{10}). In each panel, the different stages of the cell cycle are highlighted as they project into the space of this graph. **B,** Fraction of cells (y-axis) shown in **A** in each cell-cycle stage. Error bars, mean ± SD. **C,** Live-cell imaging of A375-S cells treated with DMSO or CX-6258 at indicated doses. Each row represents a single-cell track over time (x-axis in frames, images taken every 10 minutes). For each condition, two plots are shown. The right plot indicates cell divisions, where changes in color (i.e., from blue to green to orange) indicates a cell division. x-axis indicates the chronologically collected number of frames. To the left, intensity in Geminin reporter (mCherry), where accumulation of Geminin (increasing intensity indicated by red color) indicates progression toward a cell division. **D,** Fraction of micronuclei containing A375-S (y-axis) after 48-hour treatment with CX-6258 at indicated doses (x-axis; error bars, mean ± SD; DMSO vs. 0.1 μmol/L, $P_{adj} = 0.01$, DMSO vs. 0.3 μmol/L, $P_{adj} = 0.005$, ANOVA). **E,** Merged image of immunofluorescence staining of CREST (red) and DAPI (blue). (*Continued on the following page.*)

as compared with vehicle-only controls and this reduction was most pronounced in animals receiving the phased combination (30.57% vs. 10.97% of CD4$^+$, $P_{adj} < 0.001$, ANOVA; **Fig. 4D**). In contrast, there was no significant change in Tregs in tdLNs ($P = 0.29$, ANOVA) or spleens ($P = 0.27$, ANOVA) harvested from the same animals, indicating a specific effect in the TME (Supplementary Fig. S4I). We also observed increased infiltration of IFNγ-producing CD8$^+$ T and NK cells (Supplementary Fig. S4J and S4K). These data suggest that CX-6258 modulates the immune environment in tumors to favor a more consistent response to immune checkpoint blockade. HASPIN inhibition may therefore promote antitumor activity by directly inhibiting tumor growth and also improving antitumor immunity.

HASPIN inhibition may be effective in the treatment of other human cancer contexts

To investigate the therapeutic potential for HASPIN inhibition in other human cancers, we performed a pan-cancer analysis of gene expression in The Cancer Genome Atlas. We found that HASPIN was strongly overexpressed in a wide range of cancer types (Supplementary Fig. S4L). Next, we queried the Broad Institute Dependency Map (27) for cancer cell lines dependent on HASPIN expression. Multiple myeloma cell lines (DEMETER2 dependency score -0.1, $P < 0.0001$) and Ewing sarcoma (CERES dependency score -0.8, $P < 0.0001$) were predicted to be more sensitive to inhibition of HASPIN as compared with other lineages. We therefore tested the activity of CX-6258 in nine multiple myeloma cell lines (AMO1, NCI-H929, JJN-3, KMS-20, U266, XG-1, KMS-12-BM, OPM-2, and SKMM-1) and three Ewing sarcoma cell lines (RDES, SKES1, and SKNEP1). CX-6258 inhibited cell growth in all multiple myeloma cell lines tested with EC$_{50}$ < 1 μmol/L (**Fig. 4E**). In Ewing sarcoma cell lines, CX-6258 was also active at EC$_{50}$ < 1 μmol/L (**Fig. 4F**). In addition, CX-6258 inhibited formation of Ewing sarcoma spheroids; in this assay, cells are grown on a low-adherent surface to induce formation of sarcoma spheres. In SKES1, CX-6258 prevented the formation of spheroids at 5 nmol/L; in RDES and SKNEP1 there was a significant reduction of spheroid formation at 500 nmol/L and 1 μmol/L, respectively (**Fig. 4G**). Treatment of Ewing sarcoma cell lines with CX-6258 also led to induction of IFNα1 and IFNβ1 across all lines (**Fig. 4H**). Overall, these results indicate that CX-6258 may be active in multiple human cancer cell lines, while exhibiting modest toxicity against normal tissues.

Discussion

While most patients with advanced/metastatic melanoma harboring *BRAF*$^{V600E/K}$ develop resistance to treatment with RAF/MEK inhibitors (RMI), they also become less responsive to subsequent therapies, including ICI (7–10). We show that the small-molecule CX-6258 blocks cell proliferation and induces cell death of both RMI-sensitive and RMI-resistant (RMR) BRAF-mutated melanoma lines,

most likely by inhibiting HASPIN kinase, which promotes errors in mitotic chromosome segregation. Primary human TILs and neurons differentiated *in vitro* are substantially less sensitive to CX-6258 than tumor cells, suggesting a potential therapeutic window for future clinical application. CX-6258 has *in vivo* activity in immunocompetent mice and results in significant modulation of the tumor immune environment, including reduction in Tregs and increase in cytotoxic CD8$^+$ T cells, thereby contributing to a more consistent response to immunotherapy.

CX-6258 is annotated as an inhibitor of the PIM kinase family (15). However, using unbiased kinase inhibitor profiling, we identified MYLK4 and HASPIN as additional high affinity targets of CX-6258. Overexpression of PIMs did not alter the proliferation rates of cell lines in which CX-6258 was active nor did knockdown of PIM1, PIM2, or MYLK4 alter sensitivity to CX-6258. BAD is an established downstream target of PIMs but CX-6258 did not measurably reduce pBAD levels at the doses tested, showing that CX-6258 is active on cells under conditions in which PIM signaling is still active. In contrast, knockdown of HASPIN phenocopied CX-6258 with respect to cell proliferation; HASPIN knockdown also resulted in mitotic mis-segregation and formation of micronuclei and increased the number of double-stranded DNA breaks. CX-6258 also caused dose-dependent reductions in Histone H3 phosphorylation at Threonine 3, the only known phosphorylation site dependent on HASPIN. Our data strongly suggests that HASPIN is a biologically significant target of CX-6258 in cancer cells, although they do not rule out a secondary role for PIMs or MYLK4.

Some of the other compounds we tested in this study, such as SGI-1776, have a similar affinity for HASPIN in biochemical assays compared with CX-6258, but did not demonstrate significant antitumor activity in both classical viability assays and following growth rate correction. This may be due to several factors, including the higher molecular lipophilicity potential CX-6258, retention within the cell (as indicated by yellow discoloration of cells at high concentrations representing the endogenous fluorescence signal of CX-6258), and possibly by inhibiting its own transport outside of the cell via ABC transporters, as recently reported (28).

Mitotic errors resulting from CX-6258 treatment result in formation of rupture-prone micronuclei. These micronuclei stain positive with CREST antibodies, suggesting that they arise through errors in mitotic chromosome segregation and not just DSB formation. This is consistent with a role for HASPIN in mitosis. MCF10A breast cancer cell lines exposed to ionizing radiation for 3 to 6 days also develop micronuclei as a consequence of double-stranded DNA breaks (29). Formation of micronuclei requires progression through mitosis and is not observed in cells arrested in G$_2$–M. Consistent with this result, micronuclei generated in response to HASPIN inhibition with CX-6258 required progression through mitosis, and while nondivisions may result in accumulation in DSBs, they were not the source for micronuclei. This suggests that micronuclei may evolve from different

---

(*Continued.*) The white arrow indicates a micronucleus that contains chromosomal fragments (as indicated by costaining of DNA and CREST). **F,** Representative image of A375-S cells treated with either a nontargeting siRNA (negative control; top), or a siRNA against Haspin kinase and imaged over time with chromosome bridges (middle) and resulting daughter cells with pericentric micronuclei (right). **G,** Merged immunofluorescence staining of A375-S staining for γH2AX (green) or DAPI (blue) after treatment with DMSO or CX-6258 at indicated doses. At 100 nmol/L, γH2AX staining was limited to micronuclei (white arrow); at 300 nmol/L, there was higher frequency of double-stranded DNA breaks, indicated by nuclear γH2AX staining (white arrow). **H,** Western blot analysis of total and pCHK2, total and pP53, and actin-loading controls in A375-S cells treated for 48 or 72 hours with DMSO or CX-6258 at indicated doses. There was increasing abundance of pCHK2, total, and pP53, indicating activation of the DNA damage response pathway in response to CX-6258 treatment. **I,** Fraction of micronuclei formation in cGAS-proficient UACC62-S (error bars, mean $\pm$ SD; $P < 0.001$, ANOVA). **J,** Merged immunofluorescence for cGAS (green) and nuclei (DAPI, blue) in UACC62-S following treatment with DMSO versus CX-6258 (100 nmol/L). **K,** Fraction of cGAS-positive micronuclei across all imaged UACC62-S cells (*y*-axis) following treatment with CX-6258 at indicated doses in *x*-axis or DMSO (error bars, mean $\pm$ SD; $P = 0.002$, ANOVA). **L,** Western blot analysis of total and phosphorylated STING (p-STING), cGAS, and loading controls (actin and vinculin). mRNA expression of IFNα1 (**M**) and IFNβ1 (*y*-axis; **N**) in parental CT26 cell lines or corresponding CT26 cGAS-KO (*y*-axis) following treatment with CX-6258 or DMSO (error bars, mean $\pm$ SD; $P < 0.001$, statistical test, ANOVA). *, $P < 0.05$; ***, $P < 0.001$; ns, nonsignificant.
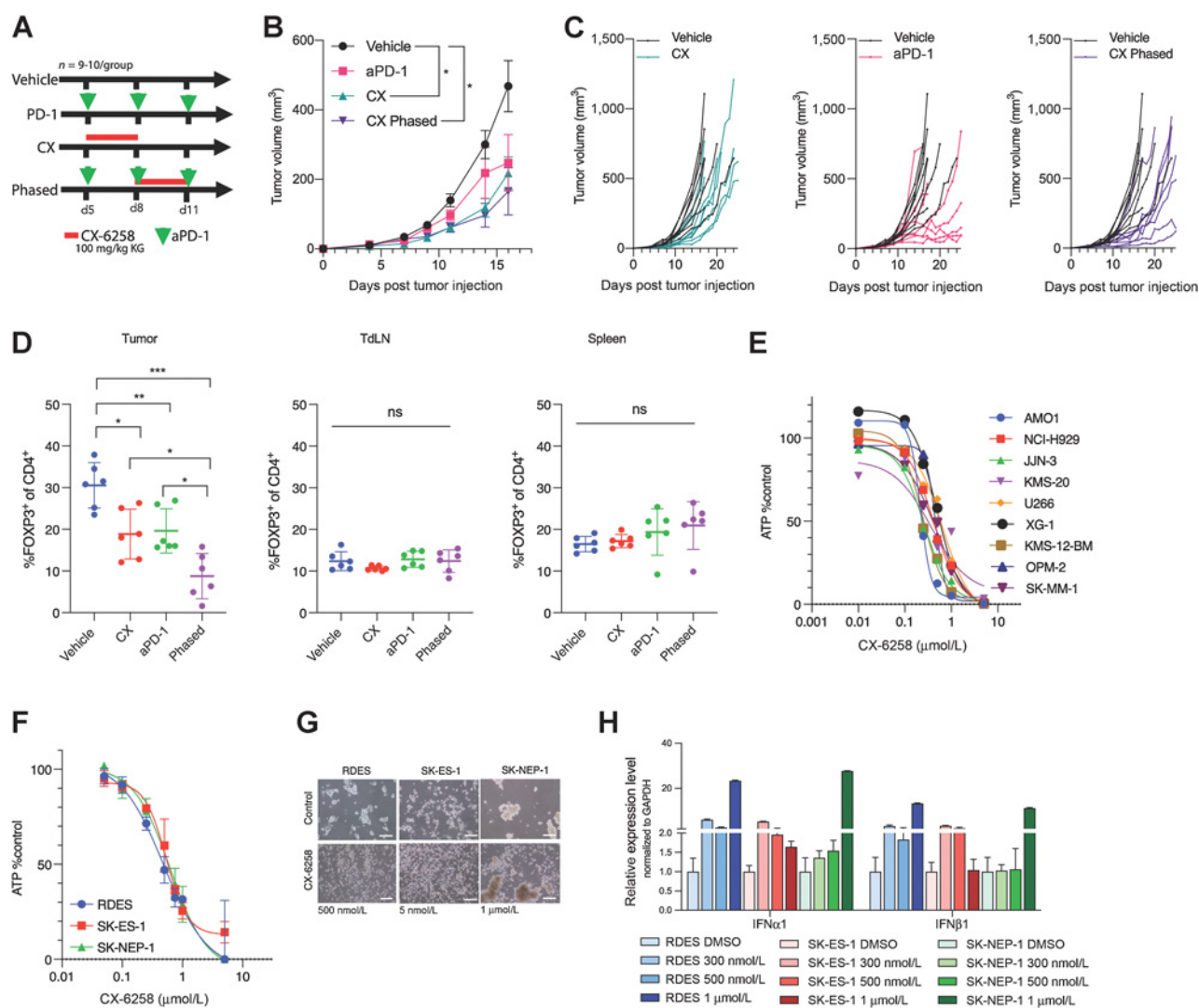
Figure 4.

A, Study design for *in vivo* in BALB/c mice implanted with CT26 tumors. Green arrowheads indicate days after tumor injection (D5, D8, and D11) animals were treated with intraperitoneally administered anti–PD-1 antibody; the red bar indicates the days animals were treated with CX-6258 by oral gavage. Top group was treated with vehicle controls, second with anti–PD-1 alone, third with CX-6258 alone, and the last group was treated with a phased combination of anti–PD-1 and CX-6258. $N = 8$ animals/group. **B,** Growth curves of animals treated per design in **A**; x-axis indicates days since tumor injection and y-axis indicates tumor volume in mm^3 (error bars, mean $\pm$ SEM; vehicle versus CX, $P_{adj} = 0.02$; vehicle vs. aPD-1, $P_{adj} = 0.36$; vehicle vs. phased, $P_{adj} = 0.002$, two-way ANOVA). **C,** Growth curves of individual animals treated per design in **A**; x-axis indicates days since tumor injection and y-axis indicates tumor volume in mm^3. **D,** Flow cytometry analysis of lymphocytes of animals implanted with CT26 tumors and treated as per treatment scheme in Supplementary Fig. S4E; x-axis indicates different treatment groups and y-axis indicates percentage of FOXP3-positive cells of all CD4$^+$ cells in tumor, tdLNs, and spleens. Analysis of $N = 6$ animals/group. (error bars, mean $\pm$ SD. $P < 0.001$, ANOVA). **E,** Multiple myeloma cell lines (names indicated on the right) treated with CX-6258; x-axis indicates doses used in μmol/L and y-axis indicates percent of ATP levels per CellTiter-Glo assay compared with DMSO-treated control. **F,** Ewing sarcoma cell lines (names indicated in bottom left) treated with CX-6258; x-axis indicates doses used in μmol/L and y-axis indicates percent of ATP activity per CellTiter-Glo assay compared with DMSO-treated control. **G,** Impact of CX-6258 treatment (right) versus DMSO (left) on spheroid formation of Ewing sarcoma cell lines shows variable responses. Scale bar, 200 μm. **H,** Relative expression of IFNα1 and IFNβ1 mRNA in Ewing sarcoma cell lines treated with increasing doses of CX-6258 (indicated by color gradient as defined at the bottom of the graph); y-axis, relative gene expression normalized to DMSO control in each cell line. *, $P < 0.05$; **, $P < 0.01$; ***, $P < 0.001$; ns, nonsignificant.

types of DNA damage, however, appear to be a result of mitotic errors during HASPIN inhibition.

Rupture of micronuclei release DNA to the cytosol, which in turn triggers the cytosolic DNA-sensor cGAS (26). We find that micronuclei recruit cGAS, as recently reported (30). While binding of cGAS to cytosolic DNA is weaker than to nuclear DNA, it has recently been reported that signaling via the cGAS–STING pathway is more potent when triggered by cytosolic DNA (31). Consistent with this finding, we see increased phosphorylation of STING, stabilization of STING, and induction of cGAS itself in response to cytosolic DNA. Chromosomal instability (CIN) resulting from errors in mitotic segregation has been associated with increased metastatic potential through tonic STING activation (32), resulting in an immunosuppressive tumor environment (33). However, acute induction of CIN as observed with CX-

6258, yields a type I IFN response and is less likely to be propagated (33). In line with this, we show that HASPIN inhibition results in a cGAS-dependent induction of type I IFN by tumor cells. This cascade promotes several changes in the tumor immune environment, including a reduction of immunosuppressive Tregs and increase in IFNγ-producing T cells, both of which are known to enhance response to ICI. Reduction of Tregs mediated by inhibitors of cell cycle or mitosis has been observed in the context of CDK4/6 inhibitors, and may indicate differential yet poorly defined sensitivity of Tregs to antiproliferative compounds (11, 34, 35), including HASPIN inhibitors.

Several inhibitors of mitotic kinases have been tested in clinical trials. Properly selected genetic subsets of tumors, such as RB1-deficient small-cell lung cancer, exhibit sensitivity to Aurora kinase B inhibitors (36), suggesting that antimitotic agents could be beneficial in the appropriate clinical context. However, Aurora kinases are involved in multiple steps in mitosis and exhibit noncanonical activities, which may, in part, explain the broad side-effect profile in patients (37). Unlike other drug targets involved in mitosis, HASPIN has only one well-described function and our study further supports this notion.

HASPIN is broadly, and more highly, expressed in various cancer types compared with the corresponding nonmalignant tissue, both may make its inhibition relatively tumor-specific. In addition to the effects observed in melanoma cell lines, we find that HASPIN inhibition may represent a therapeutic strategy in other cancers, including myeloma and Ewing sarcoma. These findings support a role for HASPIN as a target for direct inhibition of tumor growth in addition to the potential beneficial activity in combination with ICIs.

While our study provides evidence that inhibition of HASPIN's role in mitosis is the primary mechanism to promote antiproliferative activity and enhanced immunogenicity, it is possible that other, currently unknown downstream targets of HASPIN could contribute to these effects. Furthermore, inhibition of CX-6258 targets, including PIMs and HASPIN, in different cell types could in concert explain antitumor activity. For instance, while HASPIN is the key target in tumor cells, PIM2 was recently identified as negative regulator of T-cell function (38), and its inhibition may, in part, explain enhanced production of IFNγ in CD8$^+$ T cells, as shown here. This provides rationale for developing tumor-selective inhibitors of HASPIN with PIM2-inhibitory function in T cells.

In summary, our study characterizes a potent inhibitor of HASPIN, and identifies this mitotic kinase as an interesting target for drug therapy, because it results in both direct antitumor activity and modulates the tumor microenvironment, which may enhance response to immunotherapies.

Disclosure of Potential Conflicts of Interest

Authors' Contributions

Conception and design: J.C. Melms, K.W. Wucherpfennig, P.K. Sorger, B. Izar
Development of methodology: J.C. Melms, S. Vallabhaneni, C.E. Mills, A.N.R. Cartwright, A. Luoma, A. Spektor, P.K. Sorger, B. Izar
Acquisition of data (provided animals, acquired and managed patients, provided facilities, etc.): J.C. Melms, S. Vallabhaneni, C.E. Mills, C. Yapp, E. Morelli, P. Waszyk, S. Kumar, D. Deming, N. Moret, S. Rodriguez, S. Mei, D. Schadendorf, N. Riggi
Analysis and interpretation of data (e.g., statistical analysis, biostatistics, computational analysis): J.C. Melms, S. Vallabhaneni, C.E. Mills, C. Yapp, J.-Y. Chen, P. Waszyk, D. Deming, N. Moret, K. Subramanian, M. Rogava, A.N.R. Cartwright, B. Izar
Writing, review, and/or revision of the manuscript: J.C. Melms, S. Vallabhaneni, C.E. Mills, C. Yapp, P. Waszyk, D. Deming, T.J. Brinker, D.M. Miller, A. Spektor, D. Schadendorf, N. Riggi, K.W. Wucherpfennig, P.K. Sorger, B. Izar
Administrative, technical, or material support (i.e., reporting or organizing data, constructing databases): S. Vallabhaneni, S. Kumar, N. Moret
Study supervision: B. Izar

Acknowledgments

References

1. Hodis E, Watson IR, Kryukov GV, Arold ST, Imielinski M, Theurillat J-P, et al. A landscape of driver mutations in melanoma. Cell 2012;150:251–63.
2. Akbani R, Akdemir KC, Aksoy BA, Albert M, Ally A, Amin SB, et al. Genomic classification of cutaneous melanoma. Cell 2015;161:1681–96.
3. Flaherty KT, Hodi FS, Fisher DE. From genes to drugs: targeted strategies for melanoma. Nat Rev Cancer 2012;12:349–61.
4. Flaherty KT, Puzanov I, Kim KB, Ribas A, McArthur GA, Sosman JA, et al. Inhibition of mutated, activated BRAF in metastatic melanoma. N Engl J Med 2010;363:809–19.
5. Flaherty KT, Infante JR, Daud A, Gonzalez R, Kefford RF, Sosman J, et al. Combined BRAF and MEK inhibition in melanoma with BRAF V600 mutations. N Engl J Med 2012;367:1694–703.
6. Luke JJ, Flaherty KT, Ribas A, Long GV. Targeted agents and immunotherapies: optimizing outcomes in melanoma. Nat Rev Clin Oncol 2017;14:463–82.
7. Ackerman A, Klein O, McDermott DF, Wang W, Ibrahim N, Lawrence DP, et al. Outcomes of patients with metastatic melanoma treated with immunotherapy prior to or after BRAF inhibitors. Cancer 2014;120:1695–701.

Melms et al.

8. Amini-Adle M, Khanafer N, Le-Bouar M, Duru G, Dalle S, Thomas L. Ineffective anti PD-1 therapy after BRAF inhibitor failure in advanced melanoma. BMC Cancer 2018;18:705.

9. Postow MA, Chesney J, Pavlick AC, Robert C, Grossmann K, McDermott D, et al. Nivolumab and ipilimumab versus ipilimumab in untreated melanoma. N Engl J Med 2015;372:2006–17.

10. Larkin J, Chiarion-Sileni V, Gonzalez R, Grob JJ, Cowey CL, Lao CD, et al. Combined nivolumab and ipilimumab or monotherapy in untreated melanoma. N Engl J Med 2015;373:23–34.

11. Jerby-Arnon L, Shah P, Cuoco MS, Rodman C, Su M-J, Melms JC, et al. A cancer cell program promotes T cell exclusion and resistance to checkpoint blockade. Cell 2018;175:984–97.

12. Ruscetti M, Leibold J, Bott MJ, Fennell M, Kulick A, Salgado NR, et al. NK cell-mediated cytotoxicity contributes to tumor control by a cytostatic drug combination. Science 2018;362:1416–22.

13. Pantelidou C, Sonzogni O, De Oliveria Taveira M, Mehta AK, Kothari A, Wang D, et al. PARP inhibitor efficacy depends on CD8+ T-cell recruitment via intratumoral STING pathway activation in BRCA-deficient models of triple-negative breast cancer. Cancer Discov 2019;9:722–37.

14. Falchook GS, Bastida CC, Kurzrock R. Aurora kinase inhibitors in oncology clinical trials: current state of the progress. Semin Oncol 2015;42:832–48.

15. Haddach M, Michaux J, Schwaebe MK, Pierre F, O'Brien SE, Borsan C, et al. Discovery of CX-6258. A potent, selective, and orally efficacious pan-Pim kinases inhibitor. ACS Med Chem Lett 2012;3:135–9.

16. Eswaran J, Patnaik D, Filippakopoulos P, Wang F, Stein RL, Murray JW, et al. Structure and functional characterization of the atypical human kinase haspin. Proc Natl Acad Sci U S A 2009;106:20198–203.

17. Anastassiadis T, Deacon SW, Devarajan K, Ma H, Peterson JR. Comprehensive assay of kinase catalytic activity reveals features of kinase inhibitor selectivity. Nat Biotechnol 2011;29:1039–45.

18. Hafner M, Niepel M, Chung M, Sorger PK. Growth rate inhibition metrics correct for confounders in measuring sensitivity to cancer drugs. Nat Methods 2016;13:521–7.

19. Fallahi-Sichani M, Becker V, Izar B, Baker GJ, Lin J-R, Boswell SA, et al. Adaptive resistance of melanoma cells to RAF inhibition via reversible induction of a slowly dividing de-differentiated state. Mol Syst Biol 2017;13:905.

20. Sucker A, Zhao F, Pieper N, Heeke C, Maltaner R, Stadtler N, et al. Acquired IFNγ resistance impairs anti-tumor immunity and gives rise to T-cell-resistant melanoma lesions. Nat Commun 2017;8:15440.

21. Kim H, Frederick DT, Levesque MP, Cooper ZA, Feng Y, Krepler C, et al. Downregulation of the ubiquitin ligase RNF125 underlies resistance of melanoma cells to BRAF inhibitors via JAK1 deregulation. Cell Rep 2015;11:1458–73.

22. Dai J, Higgins JMG. Haspin: a mitotic histone kinase required for metaphase chromosome alignment. Cell Cycle 2005;4:665–8.

23. Harrington EA, Bebbington D, Moore J, Rasmussen RK, Ajose-Adeogun AO, Nakayama T, et al. VX-680, a potent and selective small-molecule inhibitor of the Aurora kinases, suppresses tumor growth in vivo. Nat Med 2004;10:262–7.

24. Chen Q, Sun L, Chen ZJ. Regulation and function of the cGAS-STING pathway of cytosolic DNA sensing. Nat Immunol 2016;17:1142–9.

25. Ma F, Li B, Liu S, Iyer SS, Yu Y, Wu A, et al. Positive feedback regulation of type I IFN production by the IFN-inducible DNA sensor cGAS. J Immunol 2015;194:1545–54.

26. Ablasser A, Chen ZJ. cGAS in action: expanding roles in immunity and inflammation. Science 2019;363:pii: eaat8657.

27. Tsherniak A, Vazquez F, Montgomery PG, Weir BA, Kryukov G, Cowley GS, et al. Defining a cancer dependency map. Cell 2017;170:564–76.

28. Peterson BG, Tan KW, Osa-Andrews B, Iram SH. High-content screening of clinically tested anticancer drugs identifies novel inhibitors of human MRP1 (ABCC1). Pharmacol Res 2017;119:313–26.

29. Harding SM, Benci JL, Irianto J, Discher DE, Minn AJ, Greenberg RA. Mitotic progression following DNA damage enables pattern recognition within micro-nuclei. Nature 2017;548:466–70.

30. Liu H, Zhang H, Wu X, Ma D, Wu J, Wang L, et al. Nuclear cGAS suppresses DNA repair and promotes tumorigenesis. Nature 2018;563:131.

31. Zierhut C, Yamaguchi N, Paredes M, Luo J-D, Carroll T, Funabiki H. The cytoplasmic DNA sensor cGAS promotes mitotic cell death. Cell 2019;178:302–15.

32. Bakhoum SF, Ngo B, Laughney AM, Cavallo J-A, Murphy CJ, Ly P, et al. Chromosomal instability drives metastasis through a cytosolic DNA response. Nature 2018;553:467–72.

33. Bakhoum SF, Cantley LC. The multifaceted role of chromosomal instability in cancer and its microenvironment. Cell 2018;174:1347–60.

34. Goel S, DeCristo MJ, Watt AC, BrinJones H, Sceneay J, Li BB, et al. CDK4/6 inhibition triggers anti-tumour immunity. Nature 2017;548:471–5.

35. Deng J, Wang ES, Jenkins RW, Li S, Dries R, Yates K, et al. CDK4/6 inhibition augments antitumor immunity by enhancing T-cell activation. Cancer Discov 2018;8:216–33.

36. Oser MG, Fonseca R, Chakraborty AA, Brough R, Spektor A, Jennings RB, et al. Cells lacking the RB1 tumor suppressor gene are hyperdependent on Aurora B kinase for survival. Cancer Discov 2019;9:230–47.

37. Melichar B, Adenis A, Lockhart AC, Bennouna J, Dees EC, Kayaleh O, et al. Safety and activity of alisertib, an investigational aurora kinase A inhibitor, in patients with breast cancer, small-cell lung cancer, non-small-cell lung cancer, head and neck squamous-cell carcinoma, and gastro-oesophageal adenocarcinoma: a five-arm phase 2 study. Lancet Oncol 2015;16:395–405.

38. Daenthanasanmak A, Wu Y, Iamsawat S, Nguyen HD, Bastian D, Zhang M, et al. PIM-2 protein kinase negatively regulates T cell responses in transplantation and tumor immunity. J Clin Invest 2018;128:2787–801.

Cancer Research

The Journal of Cancer Research (1916–1930) | The American Journal of Cancer (1931–1940)

AAGR American Association for Cancer Research

Inhibition of Haspin Kinase Promotes Cell-Intrinsic and Extrinsic Antitumor Activity

Johannes C. Melms, Sreeram Vallabhaneni, Caitlin E. Mills, et al.

Updated version	Access the most recent version of this article at: doi:10.1158/0008-5472.CAN-19-2330
Supplementary Material	Access the most recent supplemental material at: http://cancerres.aacrjournals.org/content/suppl/2019/12/27/0008-5472.CAN-19-2330.DC1

Cited articles	This article cites 38 articles, 7 of which you can access for free at: http://cancerres.aacrjournals.org/content/80/4/798.full#ref-list-1
Citing articles	This article has been cited by 2 HighWire-hosted articles. Access the articles at: http://cancerres.aacrjournals.org/content/80/4/798.full#related-urls

E-mail alerts	Sign up to receive free email-alerts related to this article or journal.
Reprints and Subscriptions	To order reprints of this article or to subscribe to the journal, contact the AACR Publications Department at pubs@aacr.org.
Permissions	To request permission to re-use all or part of this article, use this link http://cancerres.aacrjournals.org/content/80/4/798. Click on "Request Permissions" which will take you to the Copyright Clearance Center's (CCC) Rightslink site.